

# Nb-Based Nb-Al-Fe Alloys: Solidification Behavior and High-Temperature Phase Equilibria



FRANK STEIN and NOAH PHILIPS

High-melting Nb-based alloys hold significant promise for the development of novel high-temperature materials for structural applications. In order to understand the effect of alloying elements Al and Fe, the Nb-rich part of the ternary Nb-Al-Fe system was investigated. A series of Nb-rich ternary alloys were synthesized from high-purity Nb, Al, and Fe metals by arc melting. Solidification paths were identified and the liquidus surface of the Nb corner of the ternary system was established by analysis of the as-melted microstructures and thermal analysis. Complementary analysis of heat-treated samples yielded isothermal sections at 1723 K and 1873 K (1450 °C and 1600 °C).

DOI: 10.1007/s11661-017-4334-0

© The Author(s) 2017. This article is an open access publication

## I. INTRODUCTION

NB-BASED intermetallic alloys have been of considerable interest for structural applications at very high temperatures.<sup>[1–13]</sup> The basic concept relies on obtaining a multiphase microstructure consisting of the Nb solid solution and a high-melting, strengthening intermetallic phase (or phases). The aluminides Nb<sub>3</sub>Al and Nb<sub>2</sub>Al have been reported as interesting candidates due to both high-temperature strength and the potential to form a protective alumina scale, but respective alloys with further additions of Ti, V, Cr, or Hf were found to suffer from microstructural instability or internal oxidation with precipitation of alumina.<sup>[3,5]</sup> The present work focuses on an investigation of the combined alloying effect of Al and Fe. It appears that the simultaneous addition of Fe and Al increases the solubility limit in the Nb solid solution as well as expands the Nb<sub>2</sub>Al phase field.<sup>[14]</sup> To support the development of Nb-based intermetallics, the Nb-rich corner of the ternary Nb-Al-Fe system was investigated with a focus on solidification paths, high-temperature phase equilibria, and expanded ternary solubilities.

In a preceding study, the Nb-lean part of the Nb-Al-Fe system (less than 60 at. pct Nb) was investigated in detail including isothermal sections at 1273 K, 1423 K, and 1573 K (1000 °C, 1150 °C, and 1300 °C) as well as a liquidus surface projection.<sup>[14]</sup> The portion of

the ternary with Nb greater than 60 at. pct is hypothesized as no experimental data were available and other information from the literature about phase relations in the Nb corner of the system is very scarce (as was reviewed in the previous work). Isothermal sections of the ternary system were provided by Burnashova *et al.*<sup>[15]</sup> for 1073 K (800 °C) and by Raman<sup>[16]</sup> and Zelaya Bejarano<sup>[17,18]</sup> for 1273 K (1000 °C). In case of the binary phase Nb<sub>2</sub>Al, there is some contradiction in the literature. According to Raman's isothermal section, the solubility for Fe is at least 10 at. pct,<sup>[16]</sup> whereas the diagram of Burnashova *et al.* indicates a much lower solubility of about 1 to 2 at. pct.<sup>[15]</sup> Moreover, both groups report the existence of a Nb-rich ternary phase termed  $\mu'$ . This phase should exist in an ill-defined composition range near that of the  $\mu$  phase Nb<sub>6</sub>(Fe,Al)<sub>7</sub>. In both studies, no composition analyses were performed. More than 20 years later, Zelaya Bejarano<sup>[17,18]</sup> provided a revised 1273 K (1000 °C) isothermal section this time also including composition analyses by electron probe microanalysis (EPMA). The existence of the  $\mu'$  phase was not confirmed and it was excluded from the isothermal section. Instead, Zelaya Bejarano reported about another new, Nb-rich ternary phase, denoted as  $\beta$  phase, with an approximate composition Nb<sub>72</sub>Al<sub>20</sub>Fe<sub>8</sub>. The crystal structure of this phase was not analyzed. It is striking that the composition falls into the extended homogeneity range of the Nb<sub>2</sub>Al phase in Raman's isothermal section. The existence of both the  $\mu'$  and the  $\beta$  phase was excluded in the most recent experimental study of the system<sup>[14]</sup> and the high solubility for Fe in Nb<sub>2</sub>Al was confirmed up to 1573 K (1300 °C). Recently, two independent thermodynamic assessments were published by He *et al.*<sup>[19]</sup> and Guo *et al.*,<sup>[20]</sup> both modeling the complete ternary system on the basis of the experimental results of Stein *et al.*<sup>[14]</sup> However, the

FRANK STEIN is with the Max-Planck-Institut für Eisenforschung, Max-Planck-Str. 1, D 40237 Düsseldorf, Germany. Contact e-mail: stein@mpie.de NOAH PHILIPS is with ATI Specialty Alloys and Components, 1600 NE Old Salem Road, Albany, OR 97321.

Dedicated to Dr. Martin Palm on the occasion of his 60th birthday. Manuscript submitted June 30, 2017.

Article published online September 26, 2017

Nb-rich parts of the respective diagrams are provisional due to the lack of experimental data.

The goal of the present study was a systematic, experimental investigation of the Nb corner of the Nb-Al-Fe system. To this end, a series of Nb-rich ternary alloys were synthesized from high-purity Nb, Al, and Fe metals by arc melting and analyzed both in the as-melted state and after high-temperature equilibration to establish a liquidus surface and isothermal sections at 1723 K and 1873 K (1450 °C and 1600 °C).

## II. EXPERIMENTAL

Eleven ternary alloys with Nb contents above 60 at. pct were synthesized by arc melting from the pure metals (Nb: 99.99 wt pct\*, Al: 99.999 wt pct, Fe: 99.95 wt pct).

\*high-purity, very low interstitial Nb was supplied by ATI of Albany, OR

The arc-melted buttons were flipped, crushed with a hammer, and re-melted up to ten times in an effort to obtain fully homogeneous samples. The actual alloy compositions are given in Table I. Chemical analysis of selected samples yielded impurity contents of less than 100 ppm C, N, and O. Some of the alloys (Nos. 1, 3, 4, 9, and 11) contained inclusions of pure Nb that failed to completely dissolve during arc melting. Nevertheless, the remainder of such samples was found to be macroscopically homogeneous and all alloys were suitable for further study of the phase diagram.

The as-melted buttons were cut by EDM (electro-discharge machining) into several pieces for heat treatments, for preparation of metallographic sections of the as-melted material, and for the DTA experiments. Surface layers affected by the EDM cutting were removed by grinding.

Heat treatments were performed at 1723 K and 1873 K (1450 °C and 1600 °C) under Ar atmosphere after triple evacuation and Ar backfilling of the furnace. The samples were suspended with a 0.25-mm-thick Nb wire. Depending on the estimated melting temperatures, the duration of the heat treatment was varied from 1 day (alloys 1 to 3) to 2 days (alloys 4 to 5), 3 days (alloys 10 to 11), and 7 days (alloys 6 to 9) at 1723 K (1450 °C). Heat treatments at 1873 K (1600 °C) were only performed for the five Nb-rich alloys 5 to 9, because the alloys with the lower Nb contents (alloys 1 to 4) have solidus temperatures below 1873 K (1600 °C) as determined by DTA, and the alloys 10 and 11 have compositions that are expected to end in the Nb<sub>2</sub>Al single-phase field giving no additional information about phase equilibria. The heat treatment times varied between 6 h and 4 days, and all samples were then rapidly cooled inside the furnace [cooling rates >100 K/min to below 1273 K (1000 °C)].

Metallographic sections of all the as-melted and heat-treated alloys were prepared and microstructures were inspected by LOM (light optical microscopy) and SEM (scanning electron microscopy) in all cases. All alloy and phase compositions were analyzed by EPMA using a JEOL JXA-8100 instrument and applying pure Nb, Al, and Fe as standards. Phase compositions were analyzed with a beam size that probes volumes of about 1 μm<sup>3</sup>. 10 to 15 measurements were performed per phase in each sample. The relative error of the resulting compositions is 1 pct. The actual bulk compositions of the alloys were determined by averaging the EPMA results of 750 to 1000 spot analyses per sample measured in 3 to 4 rectangular grids with step sizes of 10 to 40 μm. The grids (usually 16 × 16 analysis points) were measured in representative parts of the samples.

For phase identification and to study the effect of ternary solid solubility on lattice parameters, XRD (X-ray diffraction) measurements were performed on all the as-melted alloys. The measurements were conducted in Bragg–Brentano geometry in a 2θ range from 10 to

**Table I. Arc-Melted Nb-Al-Fe Alloys: Alloy Compositions Determined by EPMA, and Primary and Subsequently Solidifying Phases Identified by Microstructure Inspection of the As-Melted Samples and XRD**

Alloy Composition				Primary Phase	Further Solidifying Phases	Phases by XRD
Alloy No.	At. Pct Nb	At. Pct Al	At. Pct Fe			
1	61.7	8.6	29.7	Nb	+ eut. Nb + μ	Nb + μ
2	64.0	15.5	20.5	Nb	+ perit. Nb <sub>2</sub> Al + (Nb + μ)	Nb + Nb <sub>2</sub> Al + μ
3	61.0	21.9	17.1	Nb/Nb <sub>2</sub> Al	+ perit. Nb <sub>2</sub> Al + μ	Nb + Nb <sub>2</sub> Al + μ
4	62.8	22.1	15.1	Nb/Nb <sub>2</sub> Al	+ perit. Nb <sub>2</sub> Al + μ	Nb + Nb <sub>2</sub> Al + μ
5	75.4	15.3	9.3	Nb	+ perit. Nb <sub>2</sub> Al + μ	Nb + Nb <sub>2</sub> Al + μ
6	79.3	15.9	4.8	Nb	+ perit. Nb <sub>2</sub> Al + very little μ	Nb + Nb <sub>2</sub> Al
7	83.7	11.1	5.2	Nb	+ perit. Nb <sub>2</sub> Al + little μ	Nb + Nb <sub>2</sub> Al + μ
8	86.8	8.8	4.4	Nb	+ very little Nb <sub>2</sub> Al + very little μ	Nb + Nb <sub>2</sub> Al + μ
9	78.8	18.2	3.0	Nb	+ perit. Nb <sub>3</sub> Al + perit. Nb <sub>2</sub> Al + little μ	Nb + Nb <sub>3</sub> Al + Nb <sub>2</sub> Al
10	67.5	29.5	3.0	Nb <sub>3</sub> Al	+ perit. Nb <sub>2</sub> Al + little eut. Nb <sub>2</sub> Al + C14	Nb <sub>3</sub> Al + Nb <sub>2</sub> Al
11	67.3	26.3	6.4	Nb <sub>3</sub> Al	+ perit. Nb <sub>2</sub> Al + little eut. Nb <sub>2</sub> Al + C14	Nb <sub>3</sub> Al + Nb <sub>2</sub> Al

Eut.: Eutectic, perit.: peritectically formed, μ denotes the phase Nb<sub>6</sub>(Fe,Al)<sub>7</sub>, and C14 is the Laves phase Nb(Fe,Al)<sub>2</sub>.

120 deg using an “X’Pert” Philips PW-1827 diffractometer with Co  $K_{\alpha 1}$  radiation ( $\lambda = 0.17890$  nm, step size 0.02 deg). Lattice parameters were calculated and refined using the programs MAUD<sup>[21]</sup> and LCLSQ,<sup>[22]</sup> and theoretical patterns of the phases were calculated with the CaRIne Crystallography software.<sup>[23]</sup>

Differential thermal analysis (DTA) was carried out up to 1993 K (1720 °C) with all alloys using a Setaram SETSYS-18 DTA instrument with a platinum/rhodium type-B thermocouple (Pt/Rh 70 pct/30 pct – Pt/Rh 94 pct/6 pct, by weight). Cylindrical samples of 3 mm diameter and height were placed in alumina crucibles and measured under an Ar atmosphere with a heating and a cooling rate of 10 K/min. Calibration measurements were performed using certified standards of pure Au, Ni, and Pd resulting in an accuracy of  $\pm 1$  K for the measured temperatures. All samples (except 1, 10, 11) were heated and cooled twice. The accuracy of the evaluated values for the liquidus temperatures is  $\pm 5$  K, and for all other reaction temperatures it is  $\pm 2$  K.

### III. RESULTS AND DISCUSSION

#### A. The As-Melted Material

##### 1. Microstructures and solidification sequence of phases

The primary crystallizing phases and solidification sequences were determined by inspection of the as-melted microstructures. A summary of all the as-solidified phases is given in Table I, some representative micrographs of the as-melted material are shown in Figures 1 and 2, and the revised liquidus surface projection is presented in Figure 3. As expected due to the high melting temperature of Nb, the primary phase in all but alloys 10 and 11 is the Nb solid solution (written as (Nb) in the following). In case of alloys 3 and 4, the alloy composition is very near to the monovariant boundary line of the (Nb) primary crystallization field and the samples also contain some areas where Nb<sub>2</sub>Al is the primary crystallizing phase (as is described in more detail below).

Alloys 1 to 4 show a continuous change in solidification behavior with increasing Al content (*i.e.*, moving from left to right at a constant Nb content of approximately 60 at. pct). Alloy 1 has a two-phase microstructure consisting of primary crystallized (Nb) dendrites surrounded by a eutectic matrix composed of (Nb) +  $\mu$  phase Nb<sub>6</sub>(Fe,Al)<sub>7</sub> (Figure 1(a)). This eutectic belongs to the monovariant line between  $e_2$  and  $U_2$  in Figure 3. In contrast to alloy 1, the primary (Nb) crystallites in alloy 2 are surrounded by peritectically formed Nb<sub>2</sub>Al (Figure 1(c)). The terminal solidifying matrix again consists of (Nb) +  $\mu$  phase. The peritectic formation of Nb<sub>2</sub>Al is described by the monovariant line between  $U_1$  and  $U_2$  in Figure 3 and the final solidification of (Nb) +  $\mu$  results from the invariant reaction  $U_2$ .

Alloys 3 and 4 are especially valuable as their compositions are very near to the boundary between the primary crystallization fields of (Nb) and Nb<sub>2</sub>Al. The microstructure of one region in alloy 4 (Figure 1(e))

is similar to that of alloy 2 containing small amounts of primary (Nb) crystallites surrounded by peritectic Nb<sub>2</sub>Al phase, while  $\mu$  phase again forms in the last step of solidification. The Nb<sub>2</sub>Al zones are thicker due to the higher Al content compared to alloy 2. Interestingly, the same as-melted alloy contains other areas with slightly lower Nb content, where primary (Nb) is no longer observed and instead Nb<sub>2</sub>Al is the primary phase; see Figure 1(g). It follows that the monovariant line  $U_1$  to  $U_2$  must be located between these two compositions within alloy 4.

The phases and solidification steps also become evident in plots of the complete sets of measured EPMA data points. These large data sets of 750 points, used to establish the overall composition, are shown in Figure 1(b, d, f, h). In the first and last examples (Figures 1(b) and (h)), all data points fall nearly on straight lines indicating two-phase microstructures: (Nb) +  $\mu$  for alloy 1, and Nb<sub>2</sub>Al +  $\mu$  for area 2 of alloy 4. The other two diagrams (Figures 1(d) and (f)) delineate the three-phase field (Nb) + Nb<sub>2</sub>Al +  $\mu$  observed in the respective micrographs in Figure 1. In case of area 1 in alloy 4, from Figure 1(f) it can be observed that there are no points along the connection between (Nb) and  $\mu$ . In this case, there is no contact between the (Nb) and  $\mu$  phases due to the thick, peritectically formed Nb<sub>2</sub>Al layer surrounding the primary (Nb) phase (Figure 1(e)).

The microstructures of alloys 5 to 8 all are composed of primary (Nb) surrounded by peritectically formed Nb<sub>2</sub>Al and finally solidifying  $\mu$  phase. Due to the increasing Nb content from alloy 5 to 8, the fractions of Nb<sub>2</sub>Al and  $\mu$  phase decrease in this series of alloys as can be seen in the XRD patterns; see the next section. In alloy 9, again (Nb) is the primary crystallizing phase, but this time—due to its composition near the binary Nb-Al boundary—Nb<sub>3</sub>Al instead of Nb<sub>2</sub>Al has formed as the peritectic phase surrounding (Nb) followed then by solidification of Nb<sub>2</sub>Al and a very small amount of  $\mu$  phase.

Alloys 10 and 11 both show primary crystallization of Nb<sub>3</sub>Al (inner, white phase in the micrograph shown in Figure 2). This phase is surrounded by large amounts of peritectic Nb<sub>2</sub>Al. In the final solidification step, a eutectic mixture of Nb<sub>2</sub>Al and the C14 Laves phase Nb(Fe,Al)<sub>2</sub> has formed.

Due to the non-equilibrium state of the as-melted material, the phases partially possess significant variations in concentration. Therefore, in some cases the type of the phases constituting the as-melted microstructures was difficult to identify solely on the basis of the composition values obtained from EPMA analysis. Unambiguous phase identification, however, was possible with the help of XRD as is described in the following section.

##### 2. Crystal structures and phase identification by XRD

Nb is a bcc metal (Strukturbericht designation *A2*, Pearson symbol *cI2*) with a lattice parameter of  $a = 0.330$  nm, Nb<sub>3</sub>Al has a simple cubic crystal structure (*A15*, *cP8*) with  $a = 0.5187$  nm, Nb<sub>2</sub>Al is tetragonal (*D8<sub>b</sub>*, *tP30*) with  $a = 0.9943$  nm and

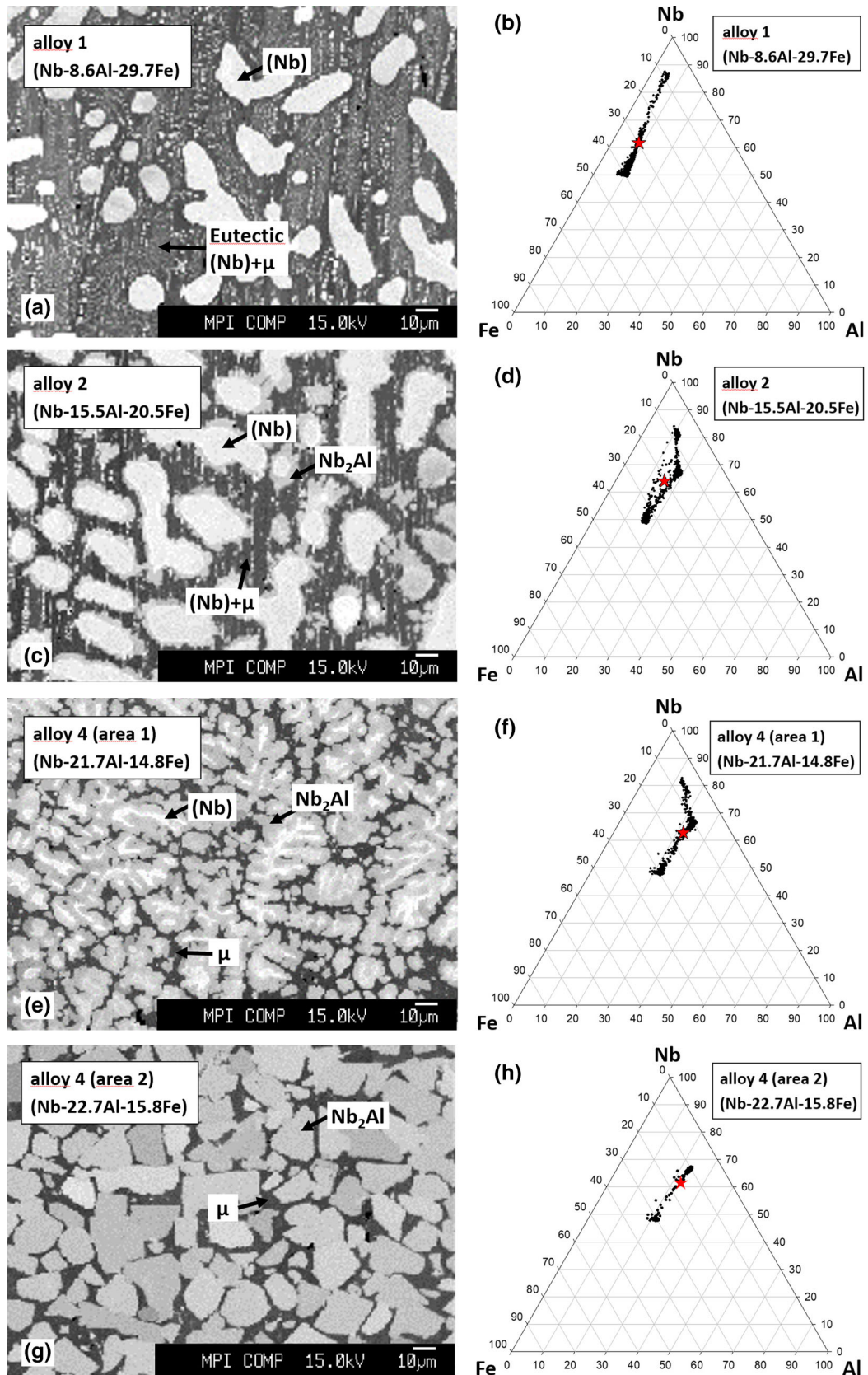


Fig. 1—(a, c, e, g) Microstructures (backscattered electron SEM micrographs) of the as-melted alloys 1, 2, and 4. (b, d, f, h) Respective composition triangles showing complete EPMA sets of measured points that were originally used for analysis of the alloy compositions (approx. 750 points per sample; the last plot showing analysis of area 2 in alloy 4 consists of 250 points). The overall sample compositions are marked by red stars (Color figure online).

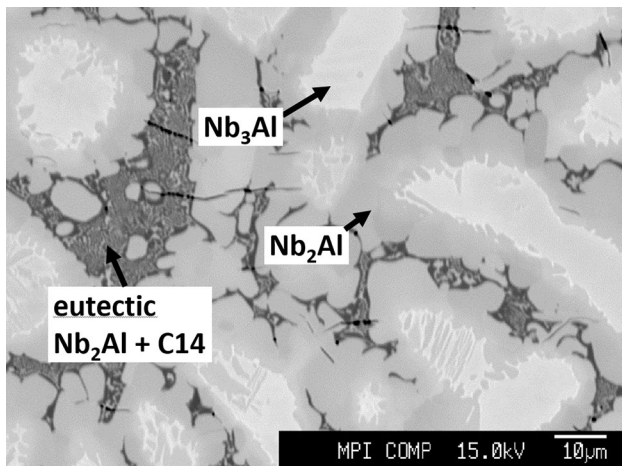


Fig. 2—Backscattered electron SEM micrograph of the as-melted alloy 11 [C14 is the Nb(Fe,Al)<sub>2</sub> Laves phase].

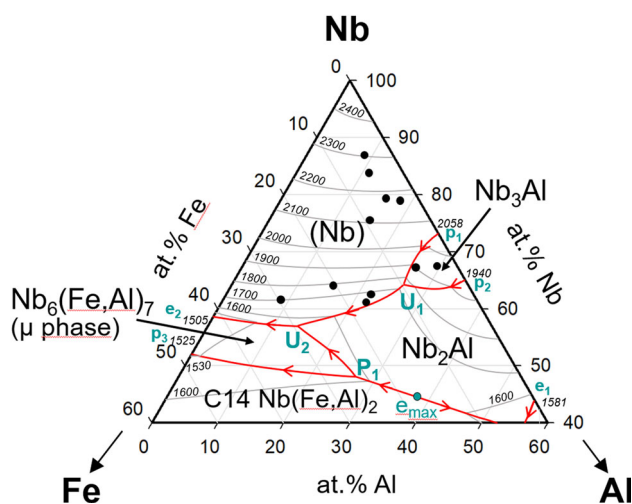


Fig. 3—Projection of the Nb corner of the liquidus surface of the Nb-Al-Fe system from this work (black circles indicate the compositions of the investigated as-melted alloys).

$c = 0.5186$  nm, and the  $\mu$  phase Nb<sub>6</sub>Fe<sub>7</sub> can be described with a hexagonal lattice (*D*8<sub>5</sub>, *h*R39) with  $a = 0.4926$  nm and  $c = 2.680$  nm. This results in very different XRD patterns making an unambiguous distinction between these phases by XRD very easy.

XRD patterns were recorded from all the as-melted samples employing the same metallographic sections that had been used for the EPMA measurements. Figure 4 shows an overview of the measured XRD patterns of the alloys 1 to 9. In all cases, all peaks could be indexed as (Nb), Nb<sub>3</sub>Al, Nb<sub>2</sub>Al, or  $\mu$  phase. The resulting phases are consistent with those found from the microstructure observations; see also Table I.

Due to the as-melted state of the samples, there is some texture in the XRD patterns though this does not pose a problem for phase identification and lattice parameter determination. The resulting lattice parameters clearly show the effect of the ternary additions. In order to allow for a comparison of this effect in the three phases (Nb), Nb<sub>3</sub>Al, and Nb<sub>2</sub>Al, the volumes per atom

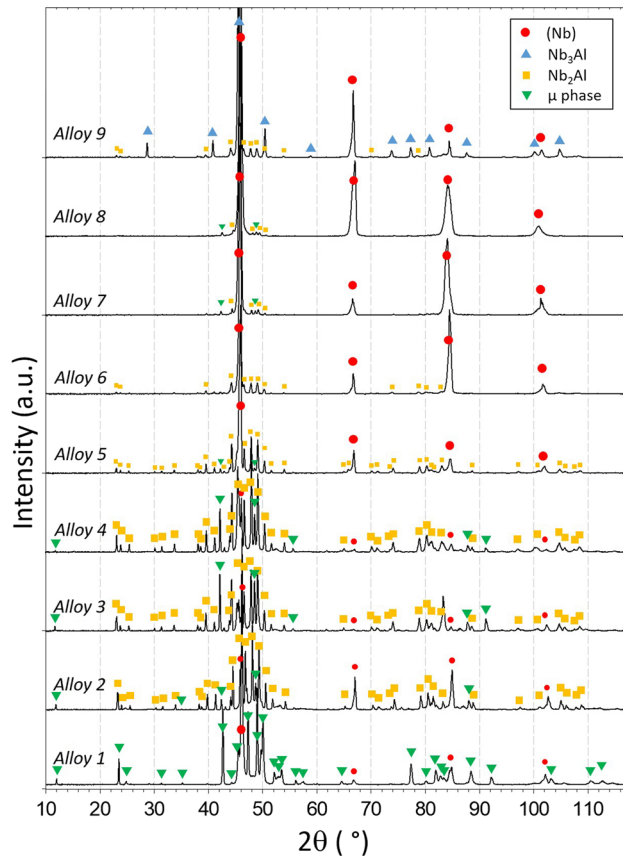


Fig. 4—XRD patterns of the as-cast alloys 1 to 9. All peaks were indexed by either (Nb), Nb<sub>3</sub>Al, Nb<sub>2</sub>Al, or Nb<sub>6</sub>Fe<sub>7</sub> ( $\mu$  phase).

were calculated from the lattice parameters and the abovementioned information about the crystal structures. The resulting data are shown in Figure 5. The scatter of the data points results from the simultaneous variation of the Al content. In addition, the non-equilibrium state of the as-melted samples might contribute to the scatter of the values. As Nb is the largest and Fe the smallest atom, the addition of Fe (and Al) leads to a decrease of the lattice parameters in all phases.

### 3. Reaction temperatures and liquidus surface

Table II shows the reaction temperatures obtained by DTA up to 1993 K (1720 °C). Several reactions related to the multistage solidification process could be measured while there were no reactions in the solid state. The liquidus temperature of alloy 1 was measured as 1973 K (1700 °C), while the solidus temperature of 1812 K (1539 °C) corresponds to the eutectic Nb +  $\mu$  line between  $e_2$  and  $U_2$ ; see Figure 3. The liquidus temperature of alloy 2 is apparently above 1993 K (1720 °C). For alloys 3 and 4, the first events on cooling, the liquidus reaction forming primary (Nb), were observed at 1947 K and 1965 K (1674 °C and 1692 °C), respectively. As the compositions of alloys 3 and 4 are very near to the monovariant line  $U_1$  to  $U_2$ , only a small amount of (Nb) is formed during primary crystallization prior to the immediately following peritectic formation of Nb<sub>2</sub>Al. Therefore, it was not possible

to resolve the two reactions. The intermediate reactions near 1843 K (1570 °C) observed in alloys 2 to 4 correspond to the formation of the  $\mu$  phase, and the solidus temperatures near 1823 K (1550 °C) are related to the invariant reaction  $U_2$ , the temperature of which was reported as 1822 K (1549 °C).<sup>[14]</sup>

Alloys 5 to 11 have higher Nb contents and no melting events were observed in these alloys up to 1993 K (1720 °C). The origin of the two weak DTA effects observed in alloys 5 and 6 may belong to the peritectic formation of  $Nb_2Al$ , but due to uncertainty these data were excluded from the construction of the liquidus surface. The reaction at 1883 K (1610 °C) observed in alloy 10 corresponds to the eutectic formation of  $Nb_2Al + C14$  and fits well to the monovariant, eutectic line in Figure 3 connecting  $P_1$  and  $E_1$  (the latter is not visible in the figure) *via* the maximum  $e_{max}$ .

Although the liquidus temperatures of the very-high-melting alloys could not be determined from the DTA experiments, the combination of all available relevant information allows prediction of the liquidus

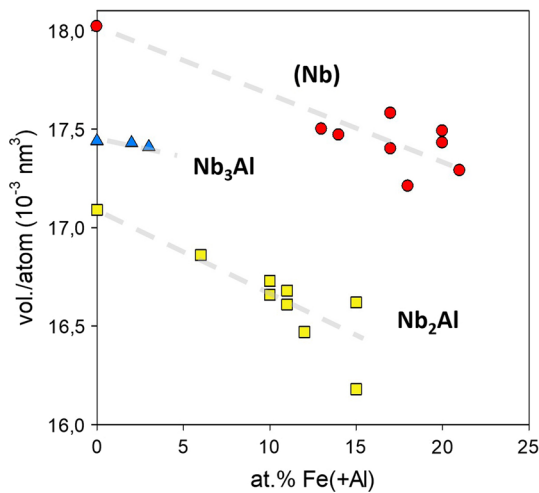


Fig. 5—Effect of dissolved Fe [or Fe+Al in case of (Nb)] on the volume per atom of the phases (Nb),  $Nb_3Al$ , and  $Nb_2Al$ .

surface. There is complete information about the primary phases and subsequent steps of solidification, which allow derivation of the position as well as type of the monovariant lines separating the primary phase fields. Moreover, the data provide information about the position and temperature of the two ternary invariant reactions  $U_1$  and  $U_2$  in the Nb corner. With respect to the preceding study,<sup>[14]</sup> position and temperature of the invariant reaction  $U_2$  are confirmed, while the position of the reaction  $U_1$  was amended and its temperature tentatively estimated as 1750 ( $\pm 50$ ) °C. As the liquidus temperatures of the binary boundary systems Al-Nb and Fe-Nb are well known from the literature (the data from the most recent assessments of He *et al.*<sup>[19,24]</sup> were used), the improved liquidus surface shown in Figure 3 was obtained from a combination of all data. The calculated liquidus surfaces reported in the recent assessments of He *et al.*<sup>[19]</sup> and Guo *et al.*<sup>[20]</sup> qualitatively agree well with the present results with the only exception of the position and temperature of the reaction  $U_1$ . In He *et al.*,<sup>[19]</sup> the point is slightly shifted to the left, *i.e.*, to lower Al contents, and a reaction temperature of 1979 K (1706 °C) is given. A strongly different result is reported in Guo *et al.*,<sup>[20]</sup> who shift the reaction point in the direction of the Al-Nb boundary and give a very high reaction temperature of 2184 K (1911 °C). For a final, precise determination of position and temperature of the reaction  $U_1$ , obviously more experimental work is still needed.

## B. Heat-Treated Material: Isothermal Sections at 1723 K and 1873 K (1450 °C and 1600 °C)

### 1. Impurities and inhomogeneities in the heat-treated microstructures

Despite the controlled atmosphere, all heat-treated samples show some degree of oxygen contamination. The depth of the affected zone varies between samples, but in all cases the transition from the outer, oxidized to the inner, uncontaminated areas occurs at a clearly visible boundary. In the interior of some samples, isolated  $Al_2O_3$  particles were found but sufficiently large

Table II. Reaction Temperatures Below 1993 K (1720 °C) from DTA Measurements

Alloy No.	Alloy Composition			Critical Temperatures from DTA	
	At. Pct Nb	At. Pct Al	At. Pct Fe	Eut./Perit. Temp. [K (°C)]	Liquidus Temperature [K (°C)]
1	61.7	8.6	29.7	1812 (1539)	1973 (1700)
2	64.0	15.5	20.5	1826, 1838, 1868 (1553, 1565, 1595)	—
3	61.0	21.9	17.1	1822, 1843 (1549, 1570)	1947 (1674)
4	62.8	22.1	15.1	1820, 1845 (1547, 1572)	1965 (1692)
5	75.4	15.3	9.3	[1910 (1637)]	—
6	79.3	15.9	4.8	[1904 (1631)]	—
7	83.7	11.1	5.2	—	—
8	86.8	8.8	4.4	—	—
9	78.8	18.2	3.0	—	—
10	67.5	29.5	3.0	1883 (1610)	—
11	67.3	26.3	6.4	—	—

The two values given in parenthesis (belonging to very weak DTA effects) were not used for the construction of the liquidus surface (see text).

**Table III. Overall and Individual Phase Compositions of Equilibrated Samples Heat-Treated at 1723 K (1450 °C), Both Determined by EPMA**

Alloy No.	Heat Treatment Time [Days]	Analyzed Overall Composition			Phases	Analyzed Phase Compositions		
		At. Pct Nb	At. Pct Al	At. Pct Fe		At. Pct Nb	At. Pct Al	At. Pct Fe
1	1	62.3	8.6	29.1	(Nb)	88.9	4.3	6.8
					$\mu$ phase	50.1	10.5	39.4
2	1	63.6	15.5	20.9	(Nb)	86.3	7.6	6.1
					Nb <sub>2</sub> Al	68.1	17.4	14.5
					$\mu$ phase	49.4	16.1	34.5
3	1	61.7	21.2	17.1	Nb <sub>2</sub> Al	67.2	21.6	11.2
					$\mu$ phase	48.4	21.2	30.4
6	7	79.1	15.6	5.3	(Nb)	86.8	9.9	3.3
					Nb <sub>3</sub> Al	78.6	19.3	2.1
					Nb <sub>2</sub> Al	69.4	22.7	7.9
7	7	84.2	10.4	5.4	(Nb)	86.7	8.8	4.5
					Nb <sub>2</sub> Al	69.2	20.1	10.7
8	7	86.2	8.0	5.8	(Nb)	86.7	7.7	5.6
					Nb <sub>2</sub> Al	68.8	18.1	13.1
9	7	78.6	18.2	3.2	(Nb)	87.0	9.7	3.3
					Nb <sub>3</sub> Al	78.7	19.2	2.1
					Nb <sub>2</sub> Al	69.5	22.4	8.1
9A	7	86.3	12.3	1.4	(Nb)	88.5	10.0	1.5
					Nb <sub>3</sub> Al	79.8	19.2	1.0
10	3	67.8	29.1	3.1	Nb <sub>2</sub> Al	67.8	29.1	3.1
10A	3	68.5	28.6	2.9	Nb <sub>3</sub> Al	77.5	21.8	0.7
					Nb <sub>2</sub> Al	68.7	28.3	3.0
11	3	67.8	25.7	6.5	Nb <sub>2</sub> Al	67.8	25.7	6.5
11A	3	72.1	23.2	4.7	Nb <sub>3</sub> Al	78.2	20.2	1.6
					Nb <sub>2</sub> Al	69.1	24.7	4.2
12*	2,1	37.1	53.4	9.5	Nb <sub>2</sub> Al	56.8	42.2	1.0
					C14	32.9	54.0	13.1
					NbAl <sub>3</sub>	24.8	74.7	0.5

Samples denoted "A" are equilibrated areas with compositions different from the main body of the alloy.

\* Taken from Stein *et al.*<sup>[14]</sup>

areas unaffected by impurities (as confirmed by EPMA) exist in all cases.

In addition to surface oxidation, some samples still contained undissolved Nb pieces from the arc melting process. In such cases, phase equilibria measurements were taken far away (*e.g.*, 1 mm) from the undissolved particles. The diffusion zone surrounding the remnant Nb particles was exploited for analysis analogous to a diffusion couple, and an example is described in the following section.

## 2. Microstructures and phase equilibria at 1723 K (1450 °C)

Despite surface oxidation, all but two samples (alloys 4 and 5 were contaminated with O and C throughout and excluded from analysis) contained sufficiently large, clean, homogeneous, and well-equilibrated areas after the heat treatments at 1723 K (1450 °C) to allow for the measurement of the equilibrium phase compositions. Table III lists the heat treatment times, the observed phases, and their compositions as well as the sample overall compositions as obtained from EPMA. Note that the overall compositions were always determined in the same area of the samples where the individual phase compositions were analyzed.

Examples for the different types of observed equilibrium microstructures after the 1723 K (1450 °C) heat treatments are presented in Figure 6. Due to their comparably low melting temperatures, the heat treatment time for the Fe-rich alloys 1 to 3 was restricted to 1 day. Figure 6(a) shows a representative micrograph of alloy 1 revealing the two-phase equilibrium between  $\mu$  phase and (Nb) solid solution. The three-phase equilibrium (Nb) + Nb<sub>3</sub>Al + Nb<sub>2</sub>Al was found in alloys 6 and 9, with a representative microstructure shown in Figure 6(b). Within the sample of alloy 9, an extended area with an increased Nb content was found, likely a remnant piece of Nb in the as-melted alloy. As the composition is homogeneous within this area, it could be evaluated as an independent equilibrated sample (denoted as 9A in Table III) representing the two-phase field (Nb) + Nb<sub>3</sub>Al. Figure 6(c) shows the three-phase equilibrium Nb<sub>2</sub>Al + NbAl<sub>3</sub> + C14 Laves phase of a sample taken from the preceding study,<sup>[14]</sup> where it had been heat-treated for 50 h at 1723 K (1450 °C) (denoted as alloy 12 in Table III). Alloys 10 and 11 have compositions lying in the Nb<sub>2</sub>Al single-phase field though in some areas with increased Nb content equilibria between Nb<sub>3</sub>Al and Nb<sub>2</sub>Al could be identified (denoted as areas 10A and 11A in Table III).

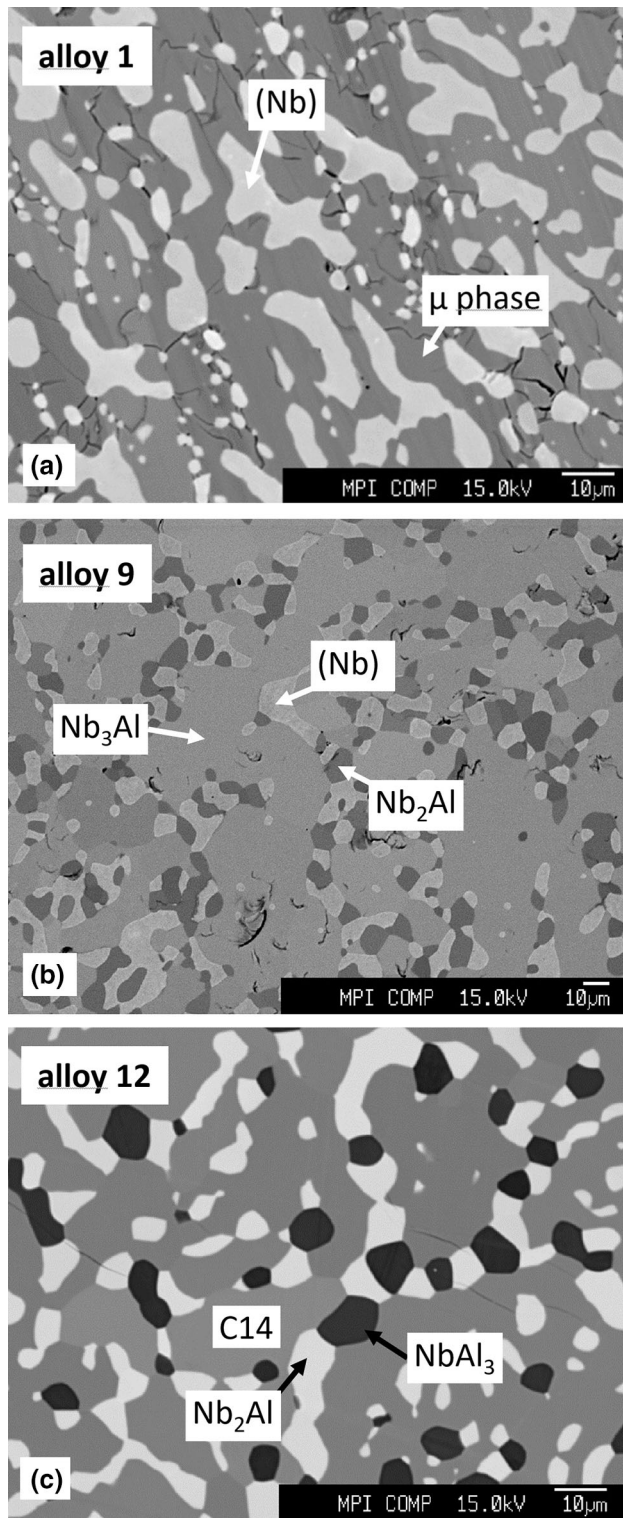


Fig. 6—Alloys 1 (a), 9 (b), and 12 (c) after heat treatment at 1723 K (1450 °C).

An example of an internal diffusion couple created by a remnant Nb piece during heat treatment is shown in Figure 7. The pure Nb piece is surrounded by an 80- $\mu\text{m}$ -thick zone of the (Nb) solid solution with continuously increasing Al + Fe content. At the point of maximum solute content, there is a discontinuous

step in the concentration profile entering the  $\text{Nb}_3\text{Al}$  zone and again at the  $\text{Nb}_3\text{Al}/\text{Nb}_2\text{Al}$  interface. Such steps represent points of local equilibrium (whereas of course within the diffusion zones the material is in a non-equilibrium state) and the respective compositions can be used like classical equilibria for drawing the phase diagram (see, e.g., Reference 25 for an introduction to the application of diffusion couples).

The ternary concentration triangle in Figure 8(a) shows all measured phase compositions including the data obtained from the internal diffusion couple described above. In addition, literature data for the binary boundary systems Al-Nb<sup>[24]</sup> and Fe-Nb<sup>[19]</sup> as well as for the ternary three-phase alloy  $\text{Nb}_2\text{Al} + \text{NbAl}_3 + \text{C14}$  Laves phase (alloy 12) from Reference 14 are considered. The resulting isothermal section (Figure 8(b)) covers all relevant two- and three-phase fields (with the exception of the Nb-poor three-phase equilibrium  $\text{Nb}_2\text{Al} + \mu + \text{C14}$  Laves phase, dotted lines in Figure 8(b)). Note that all phase compositions can be fitted by smooth lines for the phase field boundaries supporting the assumption of the existence of equilibrium in the samples.

The data well describe the extension of the  $\text{Nb}_3\text{Al}$  and  $\text{Nb}_2\text{Al}$  phase fields into the ternary system and the combined solubility of Al + Fe in the Nb solid solution. The maximum combined solubility in (Nb) reaches a value of 13.7 at. pct at this temperature, comprising 7.6 at. pct Al and 6.1 at. pct Fe. The solubility of Fe in the Nb-rich intermetallic phases is significantly higher in  $\text{Nb}_2\text{Al}$  (14.5 at. pct Fe) compared to that in  $\text{Nb}_3\text{Al}$  (2.1 at. pct Fe).

### 3. Microstructures and phase equilibria at 1873 K (1600 °C)

The overall and individual phase compositions after heat treatments at 1873 K (1600 °C) are listed in Table IV. Alloys 1 to 4 were excluded from the heat treatments as their solidus temperatures are lower than 1873 K (1600 °C), and alloys 10 and 11 were not heat-treated as they were expected to stay in the single-phase  $\text{Nb}_2\text{Al}$  composition range. Due to oxidation, some samples showed extended rim zones with oxides after the four-day heat treatments. Even though sufficiently large, clean areas remained in the center of the samples, some shifts in the chemical composition compared to the as-melted material were observed. Therefore, short-time heat treatments for 6 h at 1873 K (1600 °C) were performed with the additional samples of alloys 6 to 9 (denoted as 6' to 9').

The heat-treated sample of alloy 5 is in the two-phase equilibrium state (Nb) +  $\text{Nb}_2\text{Al}$  though this sample also contains some areas with microstructures as shown in Figure 9(a) revealing that this region was already in a partially liquid state at 1873 K (1600 °C). This is concluded from the morphology of the Nb particles and the occurrence of a large number of liquid-like droplets with fine eutectic (Nb) +  $\mu$  microstructure. This effect results from a reduction in the overall Al content (presumably due formation of  $\text{Al}_2\text{O}_3$  near the surface) shifting the composition from the (Nb) +  $\text{Nb}_2\text{Al}$  to the (Nb) + liquid two-phase field; see the isothermal section

**Table IV. Overall and Individual Phase Compositions of Equilibrated Samples Heat-Treated at 1873 K (1600 °C) as Determined by EPMA**

Alloy No.	Heat treatment Time [Days]	Analyzed Overall Composition			Phases	Analyzed Phase Compositions		
		At. Pct Nb	At. Pct Al	At. Pct Fe		At. Pct Nb	At. Pct Al	At. Pct Fe
5	1	80.1	12.6	7.3	(Nb) Nb <sub>2</sub> Al	87.3 69.5	8.5 18.5	4.2 12.0
5A	1	77.4	10.4	12.2	(Nb) $\mu$ phase	85.7 49.7	8.0 14.9	6.3 35.4
6	4	82.1	12.4	5.5	(Nb)	82.1	12.4	5.5
6A	4	78.5	15.3	6.2	(Nb) Nb <sub>2</sub> Al	81.5 68.9	13.2 22.1	5.3 9.0
6'	¼	81.4	14.9	3.7	(Nb) Nb <sub>3</sub> Al Nb <sub>2</sub> Al	86.0 77.8 69.0	10.3 19.9 23.7	3.7 2.3 7.3
7	4	90.2	6.0	3.8	(Nb)	90.2	6.0	3.8
7'	¼	84.5	10.7	4.8	(Nb)	84.5	10.7	4.8
8	4	86.3	8.7	5.0	(Nb)	86.3	8.7	5.0
8'	¼	85.5	8.9	5.6	(Nb)	85.5	8.9	5.6
9	4	83.8	15.4	0.8	(Nb) Nb <sub>3</sub> Al	86.5 79.3	12.5 20.1	1.0 0.6
9A	4	79.9	17.1	3.0	(Nb) Nb <sub>3</sub> Al Nb <sub>2</sub> Al	81.7 77.8 69.6	14.5 20.3 24.0	3.8 1.9 6.4
9'	¼	86.5	12.5	1.0	(Nb) Nb <sub>3</sub> Al	86.9 79.5	12.0 19.9	1.1 0.6
9'A	¼	82.1	14.5	3.4	(Nb) Nb <sub>3</sub> Al Nb <sub>2</sub> Al	83.6 78.2 69.8	12.3 19.8 23.5	4.1 2.0 6.7

Samples heat-treated for only 6 h are marked with a prime and "A" indicates areas with compositions different from the main body of the alloy.

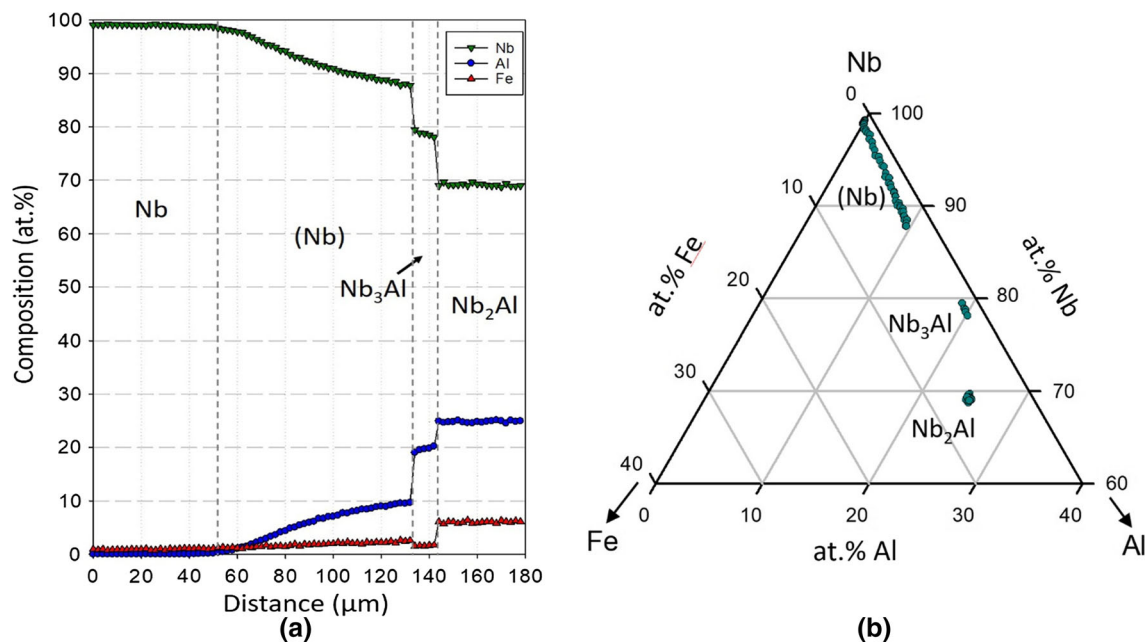


Fig. 7—(a) Concentration profile along an EPMA line scan through the diffusion zone surrounding an undissolved Nb particle in alloy 11 heat-treated at 1723 K (1450 °C) for 3 days (step size of the point analyses was 2  $\mu$ m). (b) Composition data shown in (a) plotted on the Nb-Al-Fe ternary composition triangle.

in Figure 10. The three-phase equilibrium (Nb) + Nb<sub>3</sub>Al + Nb<sub>2</sub>Al was found in samples of alloys 6 and 9, and a representative microstructure is shown in

Figure 9(b). The compositions obtained from the long-term annealings were used for construction of the three-phase triangle in the isothermal section.

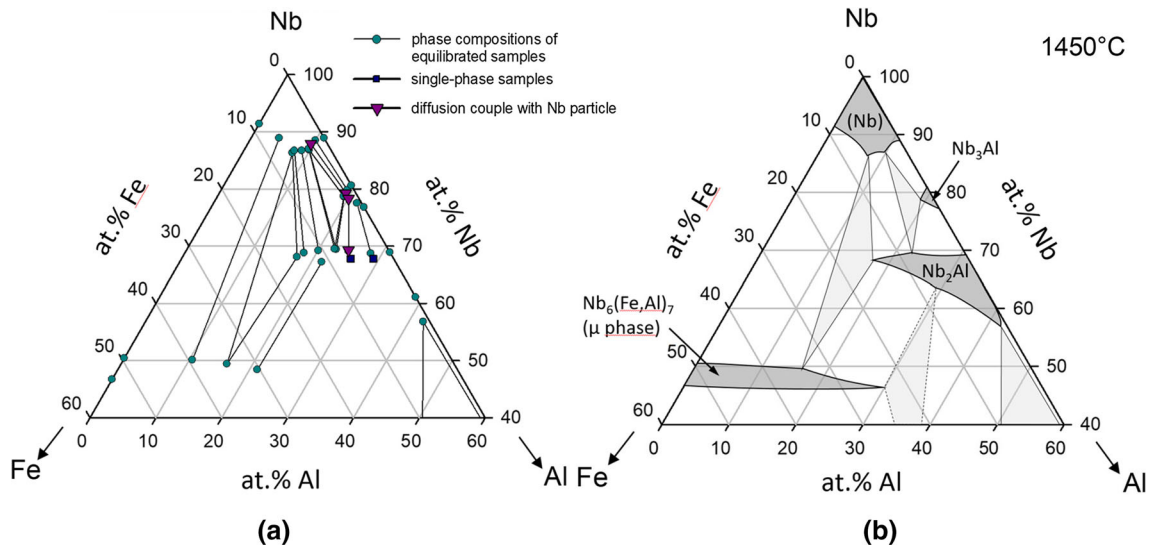


Fig. 8—(a) Experimentally determined phase equilibria at 1723 K (1450 °C) including data for the binary boundary systems taken from Refs. [19] and [24] and (b) isothermal section at 1723 K (1450 °C).

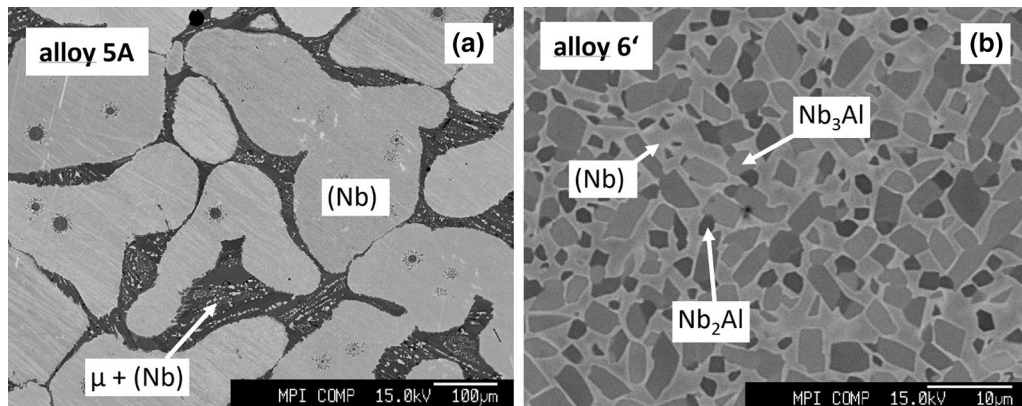


Fig. 9—Microstructures after 1873 K (1600 °C) heat treatment: (a) two-phase area (Nb) +  $\mu$  phase in alloy 5 after heat treatment for 1 day at 1873 K (1600 °C) in the partially liquid state (then consisting of (Nb) + liquid phase); (b) alloy 6' after heat treatment for 6 h at 1873 K (1600 °C) showing a (Nb) + Nb<sub>3</sub>Al + Nb<sub>2</sub>Al microstructure.

The 1873 K (1600 °C) isothermal section in Figure 10 was constructed using the experimental equilibrium data, the liquidus surface projection (Figure 3), and literature data for the binary boundary systems.<sup>[19,24]</sup> At this very high temperature, the liquid phase fields extend far into the ternary system and the phase boundaries of the liquid phase fields at 1873 K (1600 °C) can be directly read from the liquidus surface.

The maximum solubility of Al + Fe in the Nb solid solution is 18.3 at. pct (14.5 at. pct Al + 3.8 at. pct Fe). As at 1723 K (1450 °C), the solubility of Fe in the Nb-rich phase Nb<sub>3</sub>Al at 1873 K (1600 °C) is low and reaches a value of 1.9 at. pct Fe. In case of the Nb<sub>2</sub>Al phase, the Fe solubility at 1873 K (1600 °C) could not be measured as the three-phase triangle (Nb) + Nb<sub>2</sub>Al + liquid is needed. Nevertheless, from the two-phase (Nb) + Nb<sub>2</sub>Al alloy 5, it is clear that Fe solubility must be >12 at. pct. An upper limit for the solubility can be estimated from the observation that sample 5A did not contain Nb<sub>2</sub>Al. In addition, the liquid

corner of the triangle (Nb) + Nb<sub>2</sub>Al + liquid is known from the liquidus surface [composition where the 1873 K (1600 °C) isotherm cuts the monovariant line between the primary crystallization fields of (Nb) + Nb<sub>2</sub>Al, *i.e.*, the line between  $U_1$  and  $U_2$ ] and provides an upper limit for the solubility of 16 at. pct. The solubility of Fe in Nb<sub>2</sub>Al is therefore estimated as  $14 \pm 2$  at. pct, which is very similar to that at 1723 K (1450 °C) (14.5 at. pct Fe).

#### IV. SUMMARY

A detailed investigation of the Nb corner of the ternary Nb-Al-Fe phase diagram was performed. For this purpose, eleven Nb-rich ternary alloys were produced from the pure metals by arc melting. The primary crystallizing phases and solidification paths were determined from analysis of the as-melted microstructures. All phases were identified by EPMA and XRD. In addition, DTA was employed up to 1993 K (1720 °C) in

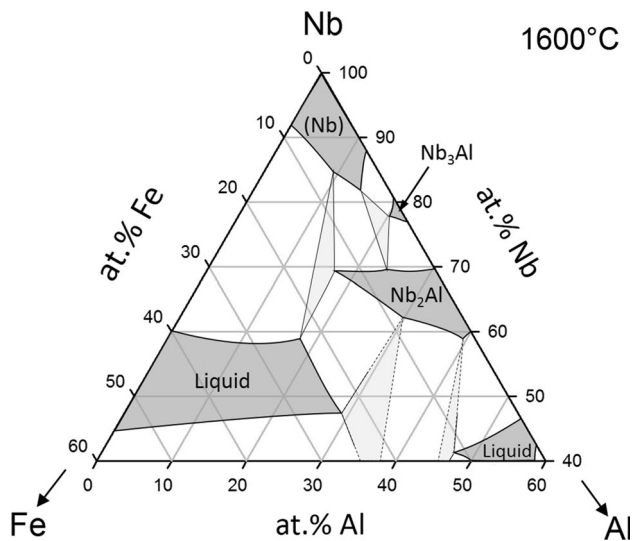


Fig. 10—Isothermal section at 1873 K (1600 °C).

order to study the liquidus temperatures and establish phase transformations below the liquidus. Combining all information, the liquidus surface of the ternary system was determined.

Heat treatments were performed at 1723 K (1450 °C) for up to 7 days and at 1873 K (1600 °C) for up to 4 days in order to obtain well-equilibrated material. Even though the heat treatments were carried out in pure Ar atmospheres, most of the samples exhibited an oxidized rim zone, but in all cases sufficiently large, clean, and homogeneous areas remained in the inner part of the samples allowing the analysis of phase equilibria. In addition, undissolved Nb particles served as internal diffusion couple providing supplemental phase equilibrium data. These results together with some information from literature were used for the construction of isothermal sections at 1723 K and 1873 K (1450 °C and 1600 °C).

### ACKNOWLEDGMENTS

Open access funding provided by Max Planck Society. The authors would like to thank Mr. M. Kulse for arc melting of the samples, Mrs. A. Bobrowski for help with metallographic preparation, Mr. G. Bialkowski for EDM cutting, and Mr. B. Breitbach for XRD measurements. Financial support by ATI is gratefully acknowledged.

### OPEN ACCESS

This article is distributed under the terms of the Creative Commons Attribution 4.0 International Li-

cense (<http://creativecommons.org/licenses/by/4.0/>), which permits unrestricted use, distribution, and reproduction in any medium, provided you give appropriate credit to the original author(s) and the source, provide a link to the Creative Commons license, and indicate if changes were made.

### REFERENCES

1. M.G. Mendiratta, J.J. Lewandowski, and D.M. Dimiduk: *Metall. Trans. A*, 1991, vol. 22A, pp. 1573–83.
2. M.G. Mendiratta and D.M. Dimiduk: *Metall. Trans. A*, 1993, vol. 24A, pp. 501–04.
3. D.M. Shah, D.L. Antonb, D.P. Pope, and S. Chin: *Mater. Sci. Eng. A*, 1995, vols. 192–193, pp. 658–72.
4. B.P. Bewlay, M.R. Jackson, and H.A. Lipsitt: *Metall. Mater. Trans. A*, 1996, vol. 27A, pp. 3801–08.
5. P.R. Subramanian, M.G. Mendiratta, and D.M. Dimiduk: *JOM*, 1996, vol. 48 (1), pp. 33–38.
6. M.R. Jackson, B.P. Bewlay, R.G. Rowe, D.W. Skelly, and H.A. Lipsitt: *JOM*, 1996, vol. 48 (1), pp. 39–44.
7. B.P. Bewlay, J.J. Lewandowski, and M.R. Jackson: *JOM*, 1997, vol. 49(8), pp. 44–45, 67.
8. B.P. Bewlay, M.R. Jackson, J.-C. Zhao, and P.R. Subramanian: *Metall. Mater. Trans. A*, 2003, vol. 34A, pp. 2043–52.
9. M. Fujikura, A. Kasama, R. Tanaka, and S. Hanada: *Mater. Trans. JIM*, 2004, vol. 45 (2), pp. 493–501.
10. S. Miura, Y. Murasatob, Y. Sekito, Y. Tsutsumi, K. Ohkubo, Y. Kimura, Y. Mishima, and T. Mohri: *Mater. Sci. Eng. A*, 2009, vol. 510, pp. 317–21.
11. J.R. Zhou and J.B. Sha: *Intermetallics*, 2013, vol. 34, pp. 1–9.
12. S. Miura, T. Hatabata, T. Okawa, and T. Mohri: *Metall. Mater. Trans. A*, 2014, vol. 45A, pp. 1136–47.
13. L. Murugesu, K.T.V. Rao, and R.O. Ritchie: *Scr. Metall. Mater.*, 1993, vol. 29 (8), pp. 1107–12.
14. F. Stein, C. He, O. Prymak, S. Voß, and I. Wossack: *Intermetallics*, 2015, vol. 59, pp. 43–58.
15. V.V. Burnashova, V.R. Ryabov, and V.Y. Markiv: *Dop. Akad. Nauk Ukr. RSR/A*, 1970, vol. 1970(8), pp. 747–50.
16. A. Raman: *Z. Metallkd.*, 1966, vol. 57, pp. 535–40.
17. J.M. Zelaya Bejarano: *Estudo do diagrama ternário ferro-alumínio-niôbio*. Estudo do diagrama ternário ferro-alumínio-niôbio, PhD thesis, Universidade Estadual de Campinas, Brazil, 1993, pp. 1–148.
18. M.A. Mota, A.A. Coelho, J.M.Z. Bejarano, S. Gama, and R. Caram: *J. Cryst. Growth*, 1999, vols. 198–199 (1), pp. 850–55.
19. C. He, Y. Qin, and F. Stein: *J. Phase Equilib. Diffus.*, 2017, vol. 38, pp. 771–87.
20. C. Guo, T. Wu, C. Li, and Z. Du: *Calphad*, 2017, vol. 57, pp. 78–87.
21. L. Lutterotti: MAUD (Materials Analysis Using Diffraction) software package, <http://maud.radiographema.eu>.
22. C.W. Burnham: *Am. Mineral.*, 1991, vol. 76 (3–4), pp. 663–64.
23. C. Boudias and D. Monceau: *Software CaRIne Crystallography*. Divergent S.A., Compiègne, France, <http://carine.crystallography.pagespro-orange.fr/index.html>.
24. C. He, F. Stein, and M. Palm: *J. Alloys Compd.*, 2015, vol. 637, pp. 361–75.
25. A.A. Kodentsov, G.F. Bastin, and F.J.J. van Loo: *Application of diffusion couples in phase diagram determination*, J.-C. Zhao, ed., *Methods for Phase Diagram Determination*, Elsevier BV, Amsterdam, The Netherlands, 2007, pp. 222–45.